

1 Modeling tabular icebergs coupled to an ocean model

A.A. Stern,¹, A. Adcroft¹ and O. Sergienko¹, G. Marquez¹, R. Hallberg¹

² **Key Points:**

³

A. A. Stern, Geophysical Fluid Dynamics Laboratory, Princeton University

A. Adcroft, Geophysical Fluid Dynamics Laboratory, Princeton University

O. Sergienko, Geophysical Fluid Dynamics Laboratory, Princeton University

G. Marquez, Geophysical Fluid Dynamics Laboratory, Princeton University

R. Hallberg, Geophysical Fluid Dynamics Laboratory, Princeton University

Abstract. The calving of giant icebergs from the Antarctic ice shelves accounts for approximately half of Antarctic ice-shelf decay. After calving these tabular icebergs drift across large distances, altering regional ocean circulation, bottom water formation and local rates biological primary productivity. Freshwater fluxes from sub-marine melting can affect large-scale sea-ice distributions, which feedback onto the greater climate system. However, despite their importance, the current generation of numerical models is unable to represent giant tabular icebergs a physically realistic way. In this study we develop novel method to model giant tabular icebergs. Tabular icebergs are constructed out of Lagrangian elements which are bonded together by numerical bonds. These numerical bonds hold the ice element together and allow the individual elements to move as a unit. By breaking these bonds, we can simulate the ocean response to giant iceberg detaching away from an ice shelf (also constructed from Lagrangian elements) or the fracturing of a large iceberg into smaller pieces. This paper provides a description and demonstration of the Lagrangian tabular-iceberg model and discusses a number of the technical elements involved its development.

1. Introduction

The Antarctic ice shelves are characterized by large infrequent calving events where massive pieces of the ice shelves break off, to create giant tabular icebergs. Observational estimates suggest that over the past 30 years approximately half of Antarctic ice-shelf decay is due to iceberg calving, while the other half occurs through ice-shelf melting [Depoorter et al , 2013; Rignot et al , 2013]. After calving, icebergs slowly drift away from their mother glaciers, often becoming stuck in sea ice, or become grounded along the Antarctic coast [Lichey and Hellmer , 2001; Dowdeswell and Bamber , 2007]. Giant tabular icebergs extend deep into the water column, and have the potential to disrupt ocean circulation patterns for months or even years after calving [Robinson et al , 2012; Stern et al , 2015]. Iceberg sizes appear to fit a power law distribution, with the majority of icebergs being small ($L < 1$ km), while the far less numerous giant tabular icebergs ($L > 5$ km) account for more than 90% of the icebergs mass [Tournadre et al , 2016].

Freshwater fluxes from iceberg melt impact ocean hydrography, influencing sea-ice production and bottom-water formation [Arrigo et al , 2002; Robinson et al , 2012; Nicholls et al , 2009]. The long distances traveled by giant icebergs before melting means that their meltwater impact is often felt hundreds of kilometers away from their calving origins [Stern et al , 2016]. Melt water injection (and the accompanying upwelling) from icebergs can also influence biological productivity by providing nutrients to the surface ocean or changing sea ice conditions [Arrigo et al , 2002; Vernet et al , 2012; Biddle et al , 2015]. The increased productivity associated with free-floating tabular icebergs has been linked

with local increases in ocean carbon uptake, potentially large enough to be a significant fraction of the Southern Ocean carbon sequestration [Smith et al , 2007].

In recent years, there has been an increased interest in iceberg drift and decay. This surge of interest has been driven by (i) the need to understand polar freshwater cycles in order to create realistic climate forecasts and sea level projections [Silva et al , 2006; Shepherd and Wingham , 2007; Rignot et al , 2013], (ii) the increased use of high-latitudes iceberg-filled waters for shipping lanes and offshore hydrocarbon exploration [Pizzolato et al , 2012; Unger , 2014; Henderson and Loe , 2016]. The increased interest in icebergs has led to the development of numerical models of iceberg drift and decay [Mountain , 1980; Bigg et al , 1997; Gladstone et al , 2001; Kubat et al , 2005], some of which have been included in global General Circulation Models [Martin and Adcroft , 2010; Marsh et al , 2015]. These iceberg models treat icebergs as Lagrangian point particles, which are advected by the flow, and melt according to certain parameterizations for icebergs melt. Since icebergs are treated as point particles, the iceberg models are mostly suitable for modeling smaller icebergs drifting across large distances, and as such iceberg models have mostly been used to represent icebergs smaller than 3.5km on a global scale [Jongma et al , 2009; Martin and Adcroft , 2010; Marsh et al , 2015]. These models are not suitable for modeling larger tabular icebergs (or smaller icebergs at fine scales), where the size and structure of the iceberg may be an important feature in determining their drift and decay [Stern et al , 2016]. They also are not suitable for studying the local effects that icebergs have on the surrounding ocean. For this reason, tabular icebergs ($L > 5\text{km}$) are currently not represented in the iceberg models used in climate models, even though observations suggest that tabular icebergs account for the vast majority of the

total Southern Hemisphere icebergs mass [Tournadre et al , 2016]. Similarly, operational iceberg models are often inadequate for projecting iceberg drift at fine scales [Turnbull et al , 2015].

The goal of this study is to develop a new iceberg model where tabular icebergs are explicitly resolved in the ocean. In this model, icebergs are no longer treated as point particles that feel the ocean at one point, but rather the icebergs have structure, depress the ocean surface, and can feel the ocean across multiple ocean grid cells. To do this, we create tabular icebergs out of many Lagrangian elements which are ‘bonded’ together by numerical bonds. The numerical bonds hold the ice elements together and allow a collection elements to move as a unit. By manually breaking these bonds, we can simulate iceberg calving, allowing us to study the ocean response to giant iceberg detaching from an ice shelf or the fracturing of a large iceberg into smaller pieces.

The discrete element model (DEM) developed in this study is referred to as the Lagrangian Tabular Iceberg Model (LTAM). Section 2 gives a description of many of the key aspects of the LTAM. Since this model is a new approach to modeling iceberg, we present many of the technical elements involved in constructing the model. In Section 3 and 4, we demonstrate the capabilities of the model by simulating a tabular iceberg detaching from an idealized ice shelf.

2. Model description

The LTAM is a Lagrangian particle-based model (or DEM model) in that the objects of the model are Lagrangian elements. Each element represents a mass of ice which is floating in the ocean, and has a position, velocity, mass, and a set of dimensions, which can evolve in time. The motion of each element is determined by a momentum equation which

is solved in the (Lagrangian) reference frame of the element. The elements are forced by oceanic and atmospheric forces, which are provided by the user, or are determined by coupling the LTAM to an ocean/atmosphere model. The elements also interact with one another and can be bonded together to form larger structures. The angular momentum of the elements is not model explicitly, instead rotational motion of larger structures emerge as a consequence of bond orientation. In different contexts, the LTAM elements can be thought to represent individual icebergs, sea ice flows, or, when the elements are bonded together, they can represent larger structures such as tabular icebergs or ice shelves.

The LTAM model is developed on the code base of an existing iceberg drift model [Martin and Adcroft , 2010; Stern et al , 2016]. When run with the correct set of runtime flags, the model runs as a traditional iceberg drift model.

2.1. Equations of motion

The elements drift in the ocean, forced by atmosphere, ocean and sea-ice drag forces, as well as the Coriolis force and a force due to the sea surface slope. When these ice elements move alone (without interactions with other elements), they can be thought of as representing individual (or clusters of) small icebergs, and follow the same equations described in the iceberg drift model of Martin and Adcroft [2010] (based on the equations outlined in Bigg et al [1997]; Gladstone et al [2001]).

In addition to the environmental forces, the elements in the LTAM model experience interactive forces due to the presence of other elements. Two types of interactive forces are included between elements. The first force is repulsive force which is applied to elements to prevent them from moving too close to one another. This repulsive force prevents icebergs from piling up on top of one another. The second interactive force is a force due

to numerical ‘bonds’, and is only applied if two elements are ‘bonded’ together. When two elements are bonded, each element feels an attractive force that prevents the elements from moving too far apart from one another. The interactive forces between two bonded elements are defined such that in the absence of other forces the elements come to rest adjacent to one another, with no overlap of the iceberg areas.

The momentum equation for each element is given by

$$M \frac{D\vec{u}}{Dt} = \vec{F}_A + \vec{F}_W + \vec{F}_R + \vec{F}_C + \vec{F}_{SS} + \vec{F}_{SI} + \vec{F}_{IA}, \quad (1)$$

where $\frac{D}{Dt}$ is the total (Lagrangian) derivative, M is the mass of the element, \vec{u} is the velocity of the element, and the terms on the right hand side give the forces on the element due to air drag (\vec{F}_A), water drag (\vec{F}_W), sea ice drag (\vec{F}_{SI}), Coriolis force (\vec{F}_C), wave radiation force (\vec{F}_R), sea surface slope (\vec{F}_{SS}), and interactions with other elements (\vec{F}_{IA}). The environmental forces are the same as those presented in Martin and Adcroft [2010], and are provided for completeness in Appendix A. The details of the interactive forces are provided in below.

2.2. Interactive Forces

The interactive force on an element is calculated by adding together the interactions with all other elements, such that the interactive force on element i , $(\vec{F}_{IA})_i$ is given by:

$$(\vec{F}_{IA})_i = \sum_{j \neq i} (\vec{F}_{IA})_{ij}, \quad (2)$$

where $(\vec{F}_{IA})_{ij}$ is the force on element i by element j . Both bonded and repulsive interactions are modeled using elastic stresses with frictional damping. The elastic component of the force is a function of the distance between the two elements, while the frictional damping force depends on the relative velocity of the two elements.

To describe the forces between two elements, we begin by introducing some notation.

Let \vec{x}_i, \vec{x}_j be the positions of elements i and j. The distance between elements i and j is

$$d_{ij} = |\vec{x}_i - \vec{x}_j|. \quad (3)$$

When calculating the interactive forces between elements, the elements are assumed to be circular. We define the interaction diameter of an element by

$$D_i = 2\sqrt{\frac{A_i}{\pi}}, \quad (4)$$

where A_i is the planar surface area of element i. Using this, we define the critical interactive length scale,

$$L_{ij} = \frac{D_i + D_j}{2}, \quad (5)$$

124 which governs interactions between elements i and j. Repulsive forces are only applied
 125 when $d_{i,j} < L_{i,j}$, while for $d_{i,j} > L_{i,j}$ attractive bonded forces are applied when a bond exists
 126 between element i and j. Bond and repulsive forces are designed such that in the absence
 127 of other forces, bonded particles will settle in an equilibrium position where elements are
 128 separated by the critical interaction length scale $L_{i,j}$.

To aid in notation, we define a bond matrix B_{ij} such that $B_{ij} = 1$ if elements i and j are bonded together and $B_{ij} = 0$ otherwise. Using this notation, the interactive force $(\vec{F}_{IA})_{ij}$ on an element i by an element j is given by

$$(\vec{F}_{IA})_{ij} = \begin{cases} (\vec{F}_e)_{ij} + (\vec{F}_d)_{ij} & \text{if } d_{ij} \leq L_{ij} \\ (\vec{F}_e)_{ij} + (\vec{F}_d)_{ij} & \text{if } d_{ij} > L_{ij} \text{ and } B_{ij} = 1 \\ 0 & \text{if } d_{ij} > L_{ij} \text{ and } B_{ij} = 0. \end{cases} \quad (6)$$

$(\vec{F}_e)_{ij}$ and $(\vec{F}_d)_{ij}$ are the elastic and frictional damping components of the interactive force between elements i and j. The elastic force $(\vec{F}_e)_{ij}$ between elements is given by

$$(\vec{F}_e)_{ij} = -\kappa_e \left(d_{i,j} - L_{i,j} \right) T_{i,j} \vec{r}, \quad (7)$$

where $\vec{r} = \frac{(\vec{x}_i - \vec{x}_j)}{|\vec{x}_i - \vec{x}_j|}$ is the directional unit vector between the position of element i and j, and κ_e is the spring constant, and $T_{i,j}$ is the minimum of the thickness of elements i, j. We choose $(\vec{F}_b)_{ij}$ proportional to $T_{i,j}$ (the minimum thickness of elements i and j) so the formulation of interactive forces has the desired property that it obeys Newton's 3rd Law (i.e.: $(\vec{F}_{IA})_{ij} = -(\vec{F}_{IA})_{ji}$). The minimum thickness is preferred to the average thickness, since this means that the for two bonded elements a fixed distance apart, acceleration due to elastic forces is bounded, even when the thickness of one of the elements approaches zero.

The frictional damping force has components that damp both the relative radial velocity and relative transverse velocities of the two elements. If \vec{r}^\perp is the direction vector perpendicular to \vec{r} , and $P_{\vec{r}}$ and $P_{\vec{r}^\perp}$ are the projection matrices that project onto \vec{r} and \vec{r}^\perp respectively, then the frictional damping force is given by

$$(\vec{F}_d)_{ij} = \left(-c_r P_{\vec{r}} - c_t P_{\vec{r}^\perp} \right) \cdot (\vec{u}_i - \vec{u}_j) \quad (8)$$

Here c_r and c_t are the radial and transverse drag coefficients. For the simulation below, we set $c_r = 2\sqrt{\kappa_e}$ and $c_t = \frac{1}{4}c_r$ so that the radial elastic force is critically damped, and the transverse damping is sub critical. The damping forces are implemented using an implicit time stepping scheme, to avoid stability issues for very small elements (details found in Appendix B).

The effectiveness of the repulsive forces can be seen in Figure 1, which shows an uncoupled (ice only) simulation where ice elements drift westward into a bay, and eventually come to rest with minimal overlap between elements. The effectiveness of the numerical bonds is demonstrated in Figure 2, where tabular icebergs (constructed from many ice elements bonded together) and individual icebergs (unbonded elements) drift together

147 towards a convex coast line. When the tabular icebergs arrive at the coast, they bump
 148 into the coastline and begin to rotate, influencing the paths of the other icebergs. In
 149 this example we see that modeling large structures using small elements bonded together,
 150 allows us to achieve large-scale structure and rotational motion, without having to include
 151 an equation for the angular momentum of the elements (as discussed in Jakobsen [2001]).
 152 Animations of these simulations can be found in the supplementary materials.

2.3. Element geometry and packing

153 For purposes of packing, we assume that elements have surface areas which are shaped
 154 as equally-sized regular hexagons (note that the elements are assumed to be circular
 155 for purposes of interactions, but are assumed to be hexagonal for packing purposes).
 156 When packing these elements together, the hexagonal elements are initially arranged in
 157 a staggered lattice, with each element bonded to the adjacent elements (see Figure 3a).
 158 In this arrangement, each element (away from the edges) is bonded to six other elements.
 159 The bonds between elements form a pattern of equilateral triangles, which give the larger
 160 structure rigidity. The circular shape of elements (used for interactions) is inscribed within
 161 the hexagonal shape used for packing (Figure 3a). The centers of adjacent elements are
 162 initially separated by a distance $d_{i,j} = L_{i,j} = 2A_p$, where A_p is the length the apothems
 163 of the hexagons.

164 Some experiments were also performed using rectangular elements, arranged in a reg-
 165 ular (non-staggered) lattice. In this case, each element forms four bonds with adjacent
 166 elements. However, the resultant structures were found to be much less rigid and tended
 167 to collapse when sufficient forces was applied. For this reason, hexagonal elements are
 168 used here.

2.4. Ocean-ice and ice-ocean coupling

The LTAM model is coupled to the ocean model via a two-way synchronous coupling, meaning that ocean model fields are passed to the LTAM model and the LTAM model fields are passed back to the ocean model at every time step. Passing fields between the two models involves interpolating fields between the Eulerian grid of the ocean model and the ‘Lagrangian grid’ of the LTAM model (i.e.: onto the ice elements).

The coupling from the ocean model to the LTAM model is straight forward: at every time step, the ocean mixed layer temperature, salinity, velocity and sea-ice concentration are passed from the ocean model to the LTAM model, to be used in the momentum and thermodynamic equations of the ice elements. Within the LTAM model, the ocean model fields are interpolated onto the Lagrangian grid using a bilinear interpolation scheme. The LTAM model is not sensitive to the chosen interpolation scheme.

The coupling in the other direction, from the LTAM model to the ocean model, is more complex. The LTAM model influences the ocean by: (i) applying a pressure to the ocean surface, (ii) applying a heat, salinity and mass flux to the ocean, associated with ice melting, and (iii) affecting the upper ocean by applying a no-slip boundary condition and frictional velocity beneath the ice. Fields from the LTAM model are interpolated from the Lagrangian grid to the Eulerian ocean grid before they are passed to the ocean model. Since the LTAM model applies large pressures to the ocean surface, the ocean model is sensitive to the interpolation scheme used to map the LTAM fields to the ocean grid. Sudden jumps to the ocean surface pressure can trigger tsunamis within the ocean model, making the ocean model become unstable.

The interpolation of the LTAM fields onto the ocean grid is done in a way that is consistent with the shape of the elements in the LTAM model (see Section 2.3). Fields are ‘spread’ to the ocean model grid by exactly calculating what fraction of an element’s surface area lies in a particular grid box, and dividing the field in proportion to this fraction. For example, consider a hexagonal element in the LTAM model, which is positioned such that it intersects four ocean grid cells (Figure 3b). In this situation, the mass of the element is divided between these four ocean cells in proportion to the overlap area between the hexagonal element and the grid cell (this fraction is shown by the colors in 3b). An advantage of this approach is that there are no jumps in pressure as an element moves from one grid cell to another.

The numerical calculation of the intersection between hexagons and the ocean grid is simplified by dividing the hexagon into 6 equilateral triangles. This method allows for the intersection to be found even when the hexagon is not aligned with the grid.

The field-spreading scheme is coded with the restriction that an element’s area can only intersect a maximum of four ocean grid cells at a time. A consequence of this is that this sets a limit on the maximum size of elements that can be represented using this model, i.e.: the longest horizontal dimension of an ice element must be smaller than the ocean grid spacing. Larger ice structures are constructed by bonding together smaller elements.

2.5. Thermodynamics

The ice elements decay according to a number of melt parameterizations. As the ice elements melt, their mass decreases, and the appropriate salt, mass and heat fluxes are passed to the ocean. In this section we described the melt parametrization for bonded, unbonded and partially bonded elements.

As mentioned above, ice elements which do not interact with other elements are modeled identically to the point particle icebergs described in Martin and Adcroft [2010]. These elements melt according to three semi-empirical parametrization for melt commonly used in previous iceberg studies [Gladstone et al , 2001; Martin and Adcroft , 2010]. Three types of iceberg melting are used: basal melt, M_b , melt due to wave erosion, M_e and melt due to buoyant convection, M_v . M_e and M_v are applied to the sides of the ice element, while M_b is applied at the ice element base. The details of M_b , M_v and M_e are given in Appendix A.

When multiple elements are bonded together to form larger structures, it is no longer appropriate to use the parameterizations for melt developed for individual point-particle icebergs. An element which is completely surrounded by other elements, is meant to represent a piece of ice in the middle of a large structure, and hence will not experience a melt at its sides due to wave erosion or buoyant convection. Also, the iceberg basal melt rate, M_b described above is based on boundary layer theory of flow past a finite plate, and is only appropriate for basal surfaces where the distance from the leading edge is sufficiently small [Eckert , 1950; Weeks and Campbell , 1973]. For an element in the interior of large structures, the distance from the edge of the structure is large, and so using M_b for the basal melt is not appropriate. Instead, the basal melt, M_s is determined using the three equation model for basal melt, which is a typical melting parametrization beneath used beneath ice shelves [Holland and Jenkins , 1999].

When using both individual elements and bonded elements in the same simulation, we determine which melt rate parameterizations to use based on the amount of bonds that each element has. An element which is in the center of a large structure will form the

maximum number of bonds, while unbonded elements form zero bonds. If maximum number of bonds that an element can form (given the shape of the element) is N_{max} , and the number bonds that an element has is N_b , then the side melt and bottom melt for that element are given by

$$M_{side} = \frac{(N_{max} - N_b)}{N_{max}}(M_v + M_e) \quad (9)$$

and

$$M_{bottom} = \frac{(N_{max} - N_b)}{N_{max}}M_b + \frac{N_b}{N_{max}}M_s \quad (10)$$

respectively. In this way, elements with no bonds, melt like point particle icebergs, elements at the center of large structures melt like ice shelves, and elements at the sides of large structures have a combination of iceberg side and basal melt, and ice-shelf melt.

2.6. Algorithms and computational efficiency

Including interactions between elements leads to an increase in the computational complexity of the model. In this subsection we comment on some of the algorithmic procedures that have been used to increase the computational efficiency.

2.6.1. Interactions and Bonds

At every time step, we calculate the force on each element due to interactions with every other element. In principle, this involves order n^2 operations (for n elements). However, since each element only has repulsive interactions with elements that are less than one ocean grid cell away, and each element only has bonded interactions with a small number of other elements, we are able to reduce the complexity of the system.

The complexity reduction is achieved by storing the element data in an efficient way that prevents having to search through all element pairs to check if they are close to

one another or are bonded with one another. The data storage system works as follows: pointers to the memory structures containing each element are stored in linked list data structures, which allow elements to be added and removed from the lists easily without restructuring the entire list. Instead of using one list for all the elements on a processor (as was done in the original code [Martin and Adcroft , 2010]), we use a separate linked list for each ocean grid cell. When an element moves between ocean grid cells, it is removed from its original list and added to the list corresponding to its new ocean grid cell. Since the area of elements has to be smaller than the area of an ocean grid cell, the critical interaction length scale (equation 5) is less than the length of a grid cell. This means that elements only experience repulsive forces with elements in the same ocean grid cell, or in one of the 8 adjacent cells. Limiting the possible repulsive interactions to elements in these 9 linked lists substantially reduces the computational time needed to calculate the total interactive force.

Bonded interactions are handled differently. Each bond is assigned a piece of memory. Each ice element contains a linked list of each of its bonds (typically up to six bonds per element). At each time step, the code traverses the lists of bonded elements, and adds a bonded force corresponding to these bond. The bonded force is only applied if $d_{i,j} > L_{ij}$, to avoid double counting an interaction. Having a list of bonds stored with each element reduces the computational complexity of bonded interactions from order n^2 to order n . Handling bonded attractive forces separately to the repulsive and non-bonded forces means that we do not need to check whether two elements are bonded, which further increases the computational efficiency.

2.6.2. Parallelization and halos

The LTAM model runs on multiple processors in parallel. When elements move from an ocean cell on one processor to an ocean cell on a second processor, the memory has to be passed from one processor the next, added and removed to the appropriate lists and the memory has to be allocated and deallocated correctly. Element interactions across the edge of processors are handled using computational halos. A computational halo is a copy of the edge of a one processor which is appended to the edge of a second processor, so that the first processor can ‘see’ the second processor during a time step. Before a time step, elements at the edges of each processor are copied onto the halos of adjacent processors so that they can be used in calculating the interactive forces. After each time step, these halos are removed, and the process is repeated. These halo updates are one of the most computationally expensive parts of the LTAM model.

Keeping track of pairs of bonded elements that move across a processor edge requires a lot of book keeping since bonds have to be severed and reconnected. Details of how the bonds are broken and reconnected across processor boundaries are provided in Appendix C.

2.6.3. Time stepping

The ice elements in the LTAM model are advected using a semi-implicit velocity Verlet time-stepping scheme. The velocity verlet time stepping scheme is commonly used in DEM models in video games because it is computational efficient and has desirable stability properties [Jakobsen , 2001]. This time stepping scheme was preferred to the Runge-Kutta 4, which was used in the iceberg model of Martin and Adcroft [2010] since, the Verlet time stepping only requires one calculation of the interactive forces per time step (while the Runge-Kutta scheme requires the interactive forces to be calculated four times).

Since the calculation of the interactive forces is one of the most computationally expensive part of the algorithm, the Verlet scheme leads to a significant increase in the speed of the model. We note that the Verlet scheme used in the LTAM contains a small modification of the original (fully explicit) velocity Verlet time stepping scheme in that damping terms are treated implicitly (which increases the numerical stability). The details of this time stepping scheme are outline in Appendix B.

3. Experiment Setup

The introduction of Lagrangian elements, numerical bonds and interpolation schemes between the Eulerian and Lagrangian grids (discussed in Section 2) means that we now have the tools to model giant tabular icebergs submerged in the ocean. We demonstrate this capability by performing a simulation of a tabular iceberg drifting away from an idealized ice shelf. This simulation is performed using the LTAM model coupled to the MOM6 ocean model [Hallberg et al , 2013].

3.1. Model configuration

We initialized our simulation using the experimental setup created for the Marine Ice Ocean Modeling Inter-comparion Project (MISOMIP) [Asay-Davis et al , 2016]. The configuration consists of an idealized ice shelf in a rectangular domain. The domain is $L_x = 80\text{km}$ wide and $L_y = 480\text{km}$ long, and contains an ice shelf which is grounded on the south side of the domain and has an ice front at $y=650\text{ km}$. The ice thickness and bottom topography of this setup are shown in Figure 4a and 4b respectively, with the grounding line position drawn in for reference. The configuration is the same as that of the Ocean0 setup in the MISOMIP, with three changes made:

1. The ‘calving criteria’ used in the MISOMIP study (which states that all points in the ice shelf with thickness less than 100m are set to zero thickness) has not been used.

2. The ice shelf has been thickened on the flanks of the domain, so that the latitude of the grounding line increases away from the center of the ice shelf.

3. The ice shelf is configured to be symmetric about its meridional center line ($x = \frac{L_x}{2}$).

This was achieved by using the average of the left and right flanks of the ice-shelf thickness.

These three changes were made in order to make the circulation beneath the ice shelf easier to interpret.

3.2. Initializing Lagrangian elements:

The idealized ice shelf is constructed out of Lagrangian ice elements. Ice elements are set to be hexagonal and are arranged in a regular staggered lattice (as discussed in Section 2.3). The sides of the gridded hexagons are initialized with length $S = 0.98$ km. Recall that the element size must be smaller than the ocean grid spacing (i.e.: $2S < \Delta x = 2$ km). Gaps along the boundaries are filled in using smaller elements so that the total ice-shelf area is preserved. The initial mass of the ice elements is determined by a preprocessing inversion step, which is the inverse of the ‘mass-spreading’ interpolation procedure discussed in Section 2.3.

Figure 4c shows what the ice-shelf draft would be if the draft were calculated from the mass of elements in each ocean grid cell without spreading an element’s mass across neighboring cells (i.e.: treating elements as point masses). Figure 4b shows the draft after spreading the mass across grid cells. When the mass spreading interpolation scheme is not used, grid artifacts seen in the ice-shelf draft (Figure 4c). The grid artifacts are much reduced when the mass spreading interpolation is used (Figure 4b).

3.3. Ocean model setup

The LTAM model is coupled to the MOM6 ocean model. The ocean model is run using vertical coordinate system which is a hybrid between a sigma-level and a z-level coordinate. In particular, model layers bend underneath the ice shelf as they would in a sigma-coordinate model, but collapse to zero thickness when they intersect with bottom topography, as they would in a z-level model. The coordinate system was achieved using ALE regridding-remapping scheme [White et al , 2009]. The model uses a horizontal resolution of 2km, and 72 vertical layers. All simulations were repeated using the ocean model run layered mode (results were similar and are not presented here). Ocean parameters are as specified in the MISOMIP configuration [Asay-Davis et al , 2016], and are shown in Table 1. The simulation is initially at rest, with horizontally uniform initial ocean temperature and salinity profiles that vary linearly between specified surface and bottom values. The initial surface temperature and salinity are $T_t = -1.9^\circ\text{C}$ and $S_t = 33.8$ psu, respectively. The initial temperature and salinity at the depth H_{ocean} are $T_b = 1.0^\circ\text{C}$ and $S_b = 34.7$ psu. The maximum ocean depth is $H_{ocean} = 720$ m. A sponge layer is used on the northern boundary, which relaxes back to the initial temperature and salinity with a relaxation time scale of $T_{sponge} = 0.1$ days. Melting is set to zero for ocean cells where the ocean column thickness is less than 10m to avoid using more energy to melt ice than is present in the water column.

3.4. Spinup and iceberg calving:

The model is spun up for 5 years with all ice elements being held stationary. After spinup, a giant tabular iceberg is 'broken off' from the ice shelf, and allowed to drift into the open ocean. This is achieved by allowing all ice elements initially within a 14.4 km

radius of the center of the ice front to move freely while the other ice elements continue to be held stationary. Ice elements less than 12 km from the center of the ice front, are bonded together to form a semi-circular tabular iceberg. A ring of elements whose distance, d , from the ice front center obeys $12 \text{ km} \leq d \leq 14.4 \text{ km}$, are allowed to move freely, but have all their bonds removed. Elements in this half annulus represent fragments of the ice shelf which calve into small pieces during a large calving event. Breaking the bonds of these surrounding elements allows the tabular iceberg to move away from the ice-shelf cavity more easily.

A wind stress $\vec{\tau} = \langle 0.05, 0.05 \rangle \frac{N}{m^2}$ is applied to drive the tabular iceberg away from the ice-shelf cavity. Perturbation experiments were performed using other wind stress values.

4. Model Results

During spinup, injection of positive buoyancy due to melting at the base of the ice shelf drives a circulation within the domain (not shown). The circulation compares well with an identical experiment run using an Eulerian ice shelf model [Goldberg et al , 2012] (a detailed comparison of the Lagrangian and Eulerian ice shelf models is presented in a separate study, and is not shown here).

After spinup, the numerical bonds are severed, and the tabular iceberg and smaller ice fragments calve away from the ice shelf and begin to move (see animations in the supplementary materials). The tabular iceberg drifts to the northward east, driven by the wind and steered by the Coriolis force (Figure 5, 6). After the iceberg has moved away from the ice shelf, we observed a warming of the surface waters nearby ice front and iceberg edge (Figure 7). This surface warming is caused by an upwelling of the warmer

waters from beneath the ice shelf and iceberg. As the icebergs drifts away from the ice front, these warmer waters remain at the surface, mapping of the wake of the iceberg (Figure 7). The signature of upwelling water in the wake of a drifting tabular iceberg bears some similarity to satellite observations of streaks of increased ocean color in the wake of tabular iceberg in the Southern Ocean [Duprat et al , 2016], suggesting that the increased productivity around iceberg may be driven by upwelling water delivering nutrients to the surface.

The motion of the tabular iceberg disturbs the ocean surface, which drives ocean velocities through out the water column (Figure 8). The elevated velocities around the tabular iceberg lead to increased vertical mixing in the vicinity of the iceberg, which alters the stratification of the water column (Figure 6), heating the upper ocean. The increased ocean velocities and increased surface temperatures cause elevated melt rates at the base of the ice shelf and iceberg (Figure 9). Large melt rates are observed at the newly calved ice-shelf front and on the rounded side of the iceberg (Figure 9a), where the iceberg calving has created steep ice cliffs. These sharp ice fronts allow for large ocean currents (Figure 9c), which drive the elevated melt rates. These elevated melt rates act to smooth out the ice front over time, making the ice cliff less steep. While this is likely a real phenomena that could be observed in nature, we should be wary of the modeled velocities at the ice cliffs, since large changes in ice thicknesses are often associated with numerical pressure gradient errors which can drive spurious motion.

As mentioned above, the direction (and speed) of the iceberg drift is largely determined by the wind speed and direction. Perturbation experiments using different wind stresses showed that for sufficiently large winds, the iceberg drifts to the north east when the

zonal component of the wind stresses is positive, and to the north west when the zonal component of the wind stress is negative. For a purely zonal wind stress with $\tau_x \leq 0.01 \frac{\text{N}}{\text{m}^2}$, the iceberg does not move away from the ice shelf. When the wind is purely offshore ($\tau_x = 0.0 \frac{\text{N}}{\text{m}^2}$), a meridional wind stress $\tau_y \geq 0.05 \frac{\text{N}}{\text{m}^2}$ is needed to move the tabular iceberg away from the ice shelf. While this result is partly an artifact of the artificial shape of the calving iceberg, it is also consistent with Bassis and Jacobs [2013] who noted that calving is a two step process consisting of (i) ice-shelf breaking and (ii) iceberg detachment. The results here suggest that strong (cross-shore) winds may be required to drive large tabular icebergs away from their mother glaciers.

Finally, we note that the numerical bonds in the LTAM model are needed in order to allow the tabular iceberg to retain its shape. Comparing the iceberg calving simulation with an identical simulation where all numerical bonds have been removed, shows that in the absence of the bonds, the ice elements quickly disperse (Figure 10). In this case, the model behavior is more similar to an ice-shelf disintegration and does not create a cohesive tabular iceberg.

5. Summary

In study above we have presented a novel method that can be used to representing tabular icebergs in numerical ocean models. In this framework, tabular icebergs (or ice shelves) are constructed out of Lagrangian particles which are held together by numerical bonds. In this way icebergs are not treated as point particles (as in previous iceberg models), but rather are explicitly resolved in the ocean. This allows the icebergs to apply pressure to the ocean surface over a wide area (larger than a grid cell), and affect circulation patterns in a way that is more physically realistic.

A demonstration of the tabular iceberg model was performed using an idealized semi-circular iceberg drifting away from an idealized ice shelf. The results showed that explicitly resolving the iceberg in the ocean allowed for a complex interaction between the tabular iceberg and the surrounding ocean. In our setup, the tabular iceberg is driven away from the ice shelf by ocean currents, wind stress, and the Coriolis force. As the iceberg moves through the water, it disturbs the ocean surface, driving barotropic ocean currents. The motion of the iceberg and melt beneath the iceberg also drive upwelling along the sides of the iceberg, which entrains ambient water and causes a warming of the surface ocean in the wake of the iceberg. The changing ocean conditions feed back onto the iceberg, affecting its motion and melt rates. The highest melt rates are observed at edge of the iceberg which has the steepest ice cliff. These have the effect of smoothing out the ice edge over time. Simulations without using numerical bonds showed that these bonds are essential for allowing the iceberg to move as a unit. We also saw that by breaking these numerical bonds we can simulate iceberg fracture, which is important process which rapidly increases the rate of iceberg decay.

The model presented here is potentially a step towards including tabular icebergs in global general climate models (GCM's). However, before this can be done, there are a number of other outstanding questions to be resolved. Firstly, it is currently unclear how and when one would introduce tabular icebergs into climate simulations, especially if the GCM does not use an active ice shelf from which the tabular icebergs can calve. For simulations with ice shelves, a calving law would be needed to decide when to release the tabular iceberg into the ocean. The question of what calving law to use is a topic of ongoing research [Benn et al , 2007; Alley et al , 2008; Levermann et al , 2012; Bassis and

Jacobs , 2013] and is still unresolved. One potential way bypass this problem would be to run hindcast simulations using historically observed calving events. Another question is how and when to break the bonds within the freely floating icebergs to simulation iceberg breakup. Without a rule for iceberg breakup, the tabular icebergs would likely drift to unrealistically low latitudes. There are also a number of outstanding questions involving the interaction between tabular icebergs and sea ice, ocean biogeochemistry and iceberg grounding. None-the-less, the technical framework described in this article is potentially a using step towards including tabular icebergs in global general climate models (GCM's).

6. Appendix A

6.1. Environmental forces on ice elements

The non-interactive forces on an ice element are as described in [Martin and Adcroft , 2010], and are repeated here for completeness. The forces on an element due to air (a), ocean (o) and sea ice (si) drag are given by

$$(\vec{F}_a) = \rho_a(0.5c_{a,v}WF + c_{a,h}LW)|\vec{u}_a - \vec{u}|(\vec{u}_a - \vec{u}), \quad (11)$$

$$(\vec{F}_o) = \rho_o(0.5c_{o,v}W(D - T_{si})F + c_{o,h}LW)|\vec{u}_o - \vec{u}|(\vec{u}_o - \vec{u}), \quad (12)$$

$$(\vec{F}_{si}) = \rho_{si}(0.5c_{si,v}WT_{si}F + c_{si,h}LW)|\vec{u}_{si} - \vec{u}|(\vec{u}_{si} - \vec{u}). \quad (13)$$

Here ρ_a , ρ_o , ρ_{si} , are the density of air, ocean and sea ice, respectively. $c_{a,v}$, $c_{o,v}$ and $c_{si,v}$ are the vertical drag coefficients with air, ocean and sea ice, while $c_{a,h}$, $c_{o,h}$ and $c_{si,h}$ are the respective horizontal drag coefficients. \vec{u}_a , \vec{u}_o , \vec{u}_{si} , are the velocities air, ocean and sea ice, respectively. L, W, T, F and D are the length, width, thickness, freeboard and draft of the ice element. The element thickness is related to the draft and freeboard by $T = F + D$ and $D = \frac{\rho}{\rho_o}T$, where ρ is the ice element density.

The wave radiation force (\vec{F}_R) is given by

$$\vec{F}_R = \frac{1}{2} \rho_o c_r g a \min(a, F) 2 \frac{WL}{W + L} \frac{\vec{v}_a}{|\vec{v}_a|} \quad (14)$$

where g is the acceleration due to gravity, a is the wave amplitude empirically related to the wind speed by $a = 0.010125|\vec{v}_a - \vec{v}_o|$, and c_{wd} is the wave drag coefficient defined as

$$c_{wd} = 0.06 \min \left(\max \left[0, \frac{L - L_c}{L_t - L_c} \right], 1 \right), \quad (15)$$

where $L_w = 0.32|\vec{v}_a - \vec{v}_o|^2$ is an empirical wave length, $L_c = 0.125L_w$ is the cutoff length, and $L_t = 0.25L_w$ is the upper limit.

The pressure gradient force is approximated as a force due to sea surface slope and given by

$$\vec{F}_{SS} = -Mg\vec{\nabla}\eta \quad (16)$$

where η is the sea surface height.

6.2. Melt rate parametrization

As discussed in Section 2.5, unbounded ice elements in the LTAM model decay according to parameterizations for iceberg decay typically used in iceberg drift models [Martin and Adcroft , 2010], while ice elements within larger ice structures have only a basal melt given by the three equation model [Holland and Jenkins , 1999] .

For unbonded ice elements, the element thickness decays due to basal melt at a rate M_b , while the length and width of the elements decay as a result of melt due to wave erosion, M_e , and melt due to buoyant convection, M_v . Following Gladstone et al [2001] and Martin and Adcroft [2010], the basal melt rate, wave erosion melt rate, and buoyant convection melt rate are parameterized by

$$M_b = 0.58|\vec{v} - \vec{v}_0|^{0.8} \frac{\tilde{T}_0 - \tilde{T}}{L^{0.2}} \quad (17)$$

$$M_e = \frac{1}{12} S_s \left(1 + \cos [\pi A_i^3] \right) \left(\tilde{T}_0 + 2 \right), \quad (18)$$

$$M_v = \left(7.62 \times 10^{-3} \right) \tilde{T}_0 + \left(1.29 \times 10^{-3} \right) \tilde{T}_0^2. \quad (19)$$

\tilde{T} is the effective iceberg temperature and is set to $\tilde{T} = 4^\circ\text{C}$, \tilde{T}_0 is the temperature at the top of the ocean, A_i is the sea ice area fraction, and S_s is the sea state, which is given by the Beaufort scale

$$S_s = \frac{2}{3} |\vec{u}_a - \vec{u}_o|^{\frac{1}{2}} + \frac{1}{10} |\vec{u}_a - \vec{u}_o| \quad (20)$$

All three melt rates are in units of meters per day.

For elements inside larger structures, the melt due to wave erosion and melt due to buoyant convection are set to zero, and the basal melt, M_s is given by the standard three equation model [Holland and Jenkins , 1999].

7. Appendix B

7.1. Modified Verlet Algorithm

The LTAM model uses a version velocity verlet time-stepping algorithm, which has been modified to allow part of the forcing to be calculated implicitly. The traditional velocity verlet algorithm is commonly used in molecular dynamics, as it is simple to implement, second order accurate and computationally efficient [Swope et al , 1982; Omelyan et al , 2002]. Here we modify the tradition scheme to allow for the drag forces to be modeled implicitly, which prevents large accelerations for element's whose mass approaches zero. To do this, we modify the traditional verlet algorithm to include both an implicit and explicit acceleration, $a = a^{exp} + a^{imp}$. The explicit acceleration, a^{exp} includes all forcing terms which depend only on the previous time step, while the implicit acceleration, a^{imp}

includes forcing terms which depend on the current time step (in particular the drag and Coriolis forces).

Using a time step of Δt , and subscripts to denote the time step (so that $t_{n+1} = t_n + \Delta t$), the modified velocity verlet scheme can be written as:

$$1) \ x_{n+1} = x_n + u_n \Delta t + \frac{1}{2} \Delta t^2 \left(a_n^{exp} + a_n^{imp} \right).$$

2) Calculate a_{n+1}^{exp} , which is a function of x_{n+1} , and other quantities measured at time t_n .

$$3) \text{ Calculate } a_{n+1}^{imp} \text{ and } u_{n+1} = u_n + \frac{\Delta t}{2} \left(a_n^{exp} + a_{n+1}^{exp} \right) + (\Delta t) a_{n+1}^{imp}$$

This scheme reduces to the traditional velocity verlet when a^{imp} is set to zero. Note that

$a_{n+1}^{exp} = a_{n+1}^{exp}(x_{n+1}, t_n)$ is an explicit function of x_{n+1} and other quantities evaluated at time

t_n , while $a_{n+1}^{imp} = a_{n+1}^{imp}(u_{n+1}, x_{n+1}, t_n)$ additionally depends on u_{n+1} , and needs to be solved

implicitly. For this reason, in step 3 a_{n+1}^{imp} and u_{n+1} need to be solved simultaneously, as

described in the next subsection.

In equation (1), the forces due to ocean drag, atmospheric drag and sea ice drag are treated implicitly. The force due to sea surface slope and wave radiation are treated explicitly. The Coriolis term is handled using Crank-Nicolson scheme so that half of the effect is implicit and half is explicit. The elastic part of the interactive forces is treated explicitly, while the interactive damping is handled semi-implicitly in that the drag force on element A by element B depends on the velocities of elements A and B evaluated at time t_{n+1} and t_n , respectively.

7.2. Solving for the velocity implicitly

Since this modified scheme contains some forcing terms which are handled implicitly, steps 2 and 3 need to be solved together. We demonstrate how this is done, using a simplified one-dimensional version of equation (1), neglecting the atmospheric drag, sea

ice drag and Coriolis force, so that the only implicitly treated term is the ocean drag. In this demonstration, we use a superscript to denote the ocean drag force, F^o and ocean velocity, u^o to avoid confusion with the subscripts indicating time step. We also define an explicit force F^{exp} , which accounts for all forces not proportional the element velocity. With these simplifications, the implicit and explicit accelerations are

$$a^{exp} = \frac{1}{M}(\vec{F}^{exp}) \quad (21)$$

$$a^{imp} = \frac{1}{M}(F^o) \quad (22)$$

The ocean drag force at time t_{n+1} is modeled (mostly) implicitly as

$$F_{n+1}^o = \tilde{c}^o |u_n^o - u_n| (u_n^o - u_{n+1}), \quad (23)$$

where \tilde{c}^o is the effective drag coefficient, accounting for the dimensions of the ice element (see equation 12).

Step 3 of the modified velocity verlet scheme can be rewritten by introducing an intermediate velocity u^* , which only depends on the velocity and acceleration at time t_n ,

$$u_n^* = u_n + \frac{1}{2}(\Delta t)a_n. \quad (24)$$

Using this, the updated velocity (Step 3) can be written

$$u_{n+1} = u_n^* + \frac{\Delta t}{2}a_{n+1}^{exp} + (\Delta t)a_{n+1}^{imp}. \quad (25)$$

Including the forcing terms into this equations gives

$$u_{n+1} = u_n^* + \frac{\Delta t}{2M}(F_{n+1}^{exp}) + \frac{\Delta t}{M}\left(c_w |u_n^o - u_n| (u_n^o - u_{n+1})\right) \quad (26)$$

Solving for $u(t_{n+1})$ in terms of quantities which only depend on the previous time step gives

$$u_{n+1} = \frac{u_n^* + \frac{\Delta t}{2M}(F_{n+1}^{exp}) + \frac{\Delta t}{M} \left(c_w |u_n^o - u_n| (u_n^o) \right)}{\left(1 + \frac{\Delta t}{M} c_w |u_n^o - u_n| \right)} \quad (27)$$

Once the u_{n+1} has been found, it can be used to calculate the explicit and implicit accelerations, which are required for the next time step.

Finally, we note that the drag term (equation 23) is not entirely implicit, since the element velocity inside the absolute value is evaluated at time t_n , rather than at time t_{n+1} . This is done so that we can solve for the updated velocity analytically. One consequence of this is that it gives rise to a small oscillation in the element velocity. This oscillation is addressed by using a predictive corrective scheme: once you have solved for a first guess of the velocity at time t_{n+1} , this estimate of the velocity is used to update the estimate of the drag force (i.e.: inside the absolute value signs). Using the updated drag, you can now repeat the process described above to find an improved estimate of the velocity. We found that two iterations were sufficient to remove the unwanted oscillation.

The procedure described in this section is easily extended to include more forcing terms and two dimensions (where it involves inverting a 2×2 matrix).

8. Appendix C

Connecting bonds across processor boundaries

Since the LTAM model can be parallelized across multiple processors, it often happens that two elements on different processes are bonded together. Keeping track of numerical bonds across processor boundaries requires a lot of book keeping. In this section we

describe the how LTAM model avoids segmentation faults by severing and reconnecting bonds at the edge of a processor during halo updates.

The basics of the bond bookkeeping work as follows: consider an element A and an element B that are bonded together. Each element has a copy of the bond (a piece of memory which describes the bond between the two elements), which is stored with the element. Let A-B be the bond stored by element A, and B-A be the bond stored by element B. Bond A-B contains a pointer which points to element B and bond B-A contains a pointer which points to element A.

Consider a situation where element A and B are originally on Processor 1, and then element B moves to Processor 2. When this occurs, the memory assigned to element B on processor 1 is removed, and is allocated on Processor 2. This means that the pointer to element B in bond A-B (stored in element A on Processor 1) is no longer assigned. Similarly, the pointer to element A in bond B-A (stored in element B on Processor 2) is no longer assigned. Before the next time step, a halo update occurs, so that there is a copy of element A in the halo of Processor 2 and a copy of element B in the halo of Processor 1. After the halo update, the bonds A-B and B-A have to be reconnected on both Processor 1 and 2. To aid in reconnecting the bonds, a copy of the grid cell number of element B is stored in the bond A-B and a copy of the grid cell number of element A is stored in the bond B-A. We refer to this as the ‘most recent address’. Before a bond is moved from one processor to another, the ‘most recent address’ is updated, so that the bond can be reconnected later. To reconnect bond A-B on Processor 1 (for example), we find the most recent address of element B, and search through the list of elements in the

539 grid cell corresponding to the most recent address of element B until element B is found.

540 The pointer to element B in bond A-B is reassigned and the bond is said to be connected.

541 Once all bonds are reconnected, a bond quality control is done where we loop through
542 all bonds and check that they are working properly. To check that a bond is working
543 properly is a four step process. For example, consider the bond A-B stored in element A
544 on Processor 1. To check the quality of this bond, we use the following four steps:

545 1. Check that the pointer to element B is assigned on bond A-B (stored on element
546 A).

547 2. Check that the corresponding bond B-A exists on element B.

548 3. Check that a pointer to element A exists in this bond B-A.

549 4. Check that the element A which is being pointed to is the same element A where
550 you started.

551 All four of these tests must pass in order to make sure that the memory is correctly
552 assigned. A useful tool in this process is that each element is assigned a unique number
553 so that elements are easily identified.

9. Possibly add

9.1. Orientation

554 Possibly add a section where we spread mass using the orientation of the icebergs.

References

- Asay-Davis, X. S., S. L. Cornford, B. K. Galton-Fenzi, R. M. Gladstone, G. H. Gudmunds-
son, D. M. Holland, P. R. Holland, and D. F. Martin (2016), Experimental design for
three interrelated marine ice sheet and ocean model intercomparison projects: MIS-
MIP v. 3 (MISMIP+), ISOMIP v. 2 (ISOMIP+) and MISOMIP v. 1 (MISOMIP1).
Geoscientific Model Development 9, no. 7: 2471.
- Arrigo, K. R., G. L. van Dijken, D. G. Ainley, M. A. Fahnestock, and T. Markus (2002).
Ecological impact of a large Antarctic iceberg. *Geophys. Res. Lett.*, 29(7).
- Alley, R. B., H. J. Horgan, I. Joughin, K. M. Cuffey, T. K. Dupont, B. R. Parizek, S.
Anandakrishnan, and J. Bassis (2008), A simple law for ice-shelf calving. *Science* 322,
no. 5906, 1344-1344.
- Bassis, J. N., and S. Jacobs (2013), Diverse calving patterns linked to glacier geometry.
Nature Geoscience, 6(10), 833-836.
- Benn, D. I., C. R. Warren, and R. H. Mottram (2007). Calving processes and the dynamics
of calving glaciers. *Earth-Science Reviews*, 82(3), 143-179.
- Bigg, G. R., Wadley, M. R., Stevens, D. P., and Johnson, J. A. (1997), Modeling the
dynamics and thermodynamics of icebergs. *Cold Regions Science and Technology*, 26(2),
113-135.
- Borstad, C. P., A. Khazendar, E. Larour, M. Morlighem, E. Rignot, M. P. Schodlok, and
H. Seroussi (2012), A damage mechanics assessment of the Larsen B ice shelf prior to
collapse: Toward a physically-based calving law, *Geophys. Res. Lett.*, 39, L18502
- Biddle, L. C., J. Kaiser, K. J. Heywood, A. F. Thompson and A. Jenkins (2015), Ocean
glider observations of iceberg-enhanced biological productivity in the northwestern Wed-

dell Sea, *Geophys. Res. Lett.*, 42, 459465.

De Rydt, J., and G. H. Gudmundsson (2016), Coupled ice shelf ocean modeling and complex grounding line retreat from a seabed ridge. *J. of Geophys. Res.: Earth Surface*, 121(5), 865-880.

Dunne, J.P., J.G. John, A.J. Adcroft, S.M. Griffies, R.W. Hallberg, E. Shevliakova, R.J. Stouffer, W. Cooke, K.A. Dunne, M.J Harrison, and J.P. Krasting (2012), GFDL's ESM2 global coupled climate-carbon Earth System Models. Part I: Physical formulation and baseline simulation characteristics. *J. of Climate*, 25(19), 6646-6665.

Depoorter, M. A., J. L. Bamber, J. A. Griggs, J. T. M. Lenaerts, Stefan RM Ligtenberg, M. R. van den Broke, and G. Moholdt (2013), Calving fluxes and basal melt rates of Antarctic ice shelves. *Nature*, 502(7469), 89-92.

Determan J., Gerdes R. (1994), Melting and freezing beneath ice shelves: implications from a three-dimensional ocean-circulation model. *Ann. Glaciol.*, 20, 413-419.

Dowdeswell, J. A., and J. L. Bamber (2007), Keel depths of modern Antarctic icebergs and implications for sea-floor scouring in the geological record. *Marine Geology*, 243(1), 120-131.

Duprat, L. P., G. R. Bigg, and D. J. Wilton (2016), Enhanced Southern Ocean marine productivity due to fertilization by giant icebergs. *Nature Geoscience*.

Eckert, E. R. G. (1950). Introduction to the Transfer of Heat and Mass. McGraw-Hill.

Gladstone, R. M., G. R. Bigg, and K. W. Nicholls. (2001), Iceberg trajectory modeling and meltwater injection in the Southern Ocean (1978-2012). *J. of Geophys. Res.: Oceans*, 106(C9), 19903-19915.

- Goldberg, D. N., C. M. Little, O. V. Sergienko, A. Gnanadesikan, R. Hallberg, and M. Oppenheimer (2012), Investigation of land ice-ocean interaction with a fully coupled ice-ocean model: 1. Model description and behavior. *J. of Geophys. Res.: Earth Surface*, 117(F2).
- Gladish, C. V., D. M. Holland, P. R. Holland, and S. F. Price (2012), Ice-shelf basal channels in a coupled ice/ocean model. *J. of Glaciol.*, 58(212), 1227-1244.
- Grosfeld K., R. Gerdes, J. Determan (1997), Thermohaline circulation and interaction between ice shelf cavities and the adjacent open ocean. *J. Phys. Oceanogr.*, **102**, C7, 15959-15610.
- Grosfeld, K., and H. Sandhger, (2004). The evolution of a coupled ice shelfocean system under different climate states. *Global and Planetary Change*, 42(1), 107-132.
- Hallberg, R., A. Adcroft, J. P. Dunne, J. P., Krasting, R. J., and Stouffer (2013), Sensitivity of twenty-first-century global-mean steric sea level rise to ocean model formulation. *J. of Climate*, 26(9), 2947-2956.
- Holland D. M., Jenkins A. (2001), Adaptation of an isopycnic coordinate ocean model for the study of circulation beneath ice shelves. *Mon. Wea. Rev.*, 129, 1905-1927.
- Holland P. R. and D. L. Feltham (2006), The effects of rotation and ice shelf topography on frazil-laden Ice Shelf Water plumes. *J. Phys. Oceanogr.*, 36, 2312-2327.
- Holland, D. M., and A. Jenkins (1999), Modeling thermodynamic ice-ocean interactions at the base of an ice shelf. *J. of Phys. Oceanogr.* 29.8, 1787-1800.
- Hellmer H.H., Olbers D. J. (1989), A two-dimensional model for the thermohaline circulation under an ice shelf. *Antarctic Science*, 1, 325- 336.

- 621 Henderson J., J. S. P. Loe (2016), The Prospects and Challenges for Arctic Oil Develop-
622 ment. *Oil, Gas and Energy Law Journal (OGEL)*, 14 (2)
- 623 Hopkins, M. A. (1996). On the mesoscale interaction of lead ice and floes. *J. of Geophys.*
624 *Res.: Oceans*, 101(C8), 18315-18326.
- 625 Gaskill, H. S., and J. Rochester (1984). A new technique for iceberg drift prediction. *Cold*
626 *Reg. Sci. Technol.*, 8(3), 223-234.
- 627 Jakobsen, T. (2001). Advanced character physics. *In Game Developers Conference*, Vol.
628 3.
- 629 Jenkins, A., P. Dutrieux, S. S. Jacobs, S. D. McPhail, J. R. Perrett, A. T. Webb, and
630 D. White (2010), Observations beneath Pine Island Glacier in West Antarctica and
631 implications for its retreat. *it Nature Geo.*, 3(7), 468-472.
- 632 Jacobs, S. S., A. Jenkins, C. F. Giulivi, and P. Dutrieux (2011). Stronger ocean circulation
633 and increased melting under Pine Island Glacier ice shelf. *Nature Geo.*, 4(8), 519-523.
- 634 Jongma, J. I., E. Driesschaert, T. Fichefet, H. Goosse, and H. Renssen (2009), The effect of
635 dynamic-thermodynamic icebergs on the Southern Ocean climate in a three-dimensional
636 model, *Ocean Modell.*, 26, 104113.
- 637 Kubat I., M. Sayed, S. Savage, T. Carrieres (2005), An operational model of iceberg drift
638 *Int. J. Off. Polar Eng.*, 15 (2), 125131
- 639 Lewis E.L. and R.G. Perkin (1986), Ice pumps and their rates. *J. of Geophys. Res.*, 91,
640 11756-11762.
- 641 Losch, M. (2008). Modeling ice shelf cavities in az coordinate ocean general circulation
642 model. *J. of Geophys. Res.: Oceans*, 113(C8).

- Li, B., H. Li, Y. Liu, A. Wang and S. Ji (2014), A modified discrete element model for sea ice dynamics. *Acta Oceanologica Sinica*, 33(1), 56-63.
- Liu, M. B. and G. R. Liu (2010), Smoothed particle hydrodynamics (SPH): an overview and recent developments. *Archives of computational methods in engineering*, 17(1), 25-76.
- Lichey, C., and H. H. Hellmer (2001). Modeling giant-iceberg drift under the influence of sea ice in the Weddell Sea, Antarctica. *J. of Glaciol.*, 47(158), 452-460.
- Levermann, A., T. Albrecht, R. Winkelmann, M. A. Martin, M. Haseloff, and I. Joughin. (2012), Kinematic first-order calving law implies potential for abrupt ice-shelf retreat. *The Cryosphere*, 6(2), 273-286.
- Mountain, D. G. (1980). On predicting iceberg drift. *Cold Reg. Sci. Technol.*, 1(3-4), 273-282.
- Martin, T., and Adcroft, A. (2010), Parameterizing the fresh-water flux from land ice to ocean with interactive icebergs in a coupled climate model. *Ocean Modelling*, 34(3), 111-124.
- Marsh, R., V. O. Ivchenko, N. Skliris, S. Alderson, G. R. Bigg, G. Madec, A. T. Blaker Y. Aksenov, B. Sinha, A.C. Coward, and J.L. Sommer (2015), NEMOICB (v1. 0): interactive icebergs in the NEMO ocean model globally configured at eddy-permitting resolution. *Geoscientific Model Development* 8, no. 5 (2015): 1547-1562.
- MacAyeal D.R. (1984), Thermohaline Circulation Below the Ross Ice Shelf: A Consequence of Tidally Induced Vertical Mixing and Basal Melting. *J. Geophys. Res.*, 89, 597-606

- 665 Nicholls K.W. (1996), Temperature variability beneath Ronne Ice Shelf, Antarctica, from
666 thermistor cables. *J. Phys. Oceanogr.*, 11, 1199-1210.
- 667 Nicholls KW, Østerhus S, Makinson K (2009), Ice-Ocean processes over the continental
668 shelf of the southern Weddell Sea, Antarctica: a review. *Rev. Geophys.* 47(3).
- 669 Omelyan, I. P., M. I. Mryglod, and R. Folk (2002), Optimized Verlet-like algorithms for
670 molecular dynamics simulations. *Physical Review E*, 65(5), 056706.
- 671 Rignot, E., S. Jacobs, J. Mouginot, and B. Scheuchl (2013), Ice-shelf melting around
672 Antarctica. *Science*, 341, no. 6143 (2013): 266-270.
- 673 Robinson, N. J., M. J. M. Williams, P. J. Barrett, and A. R. Pyne (2010), Observations of
674 flow and ice-ocean interaction beneath the McMurdo Ice Shelf, Antarctica, *J. Geophys.*
675 *Res.*, 115, C03025
- 676 Pizzolato, L., S. E. Howell, C. Derksen, J. Dawson, L. Copland (2014), Changing sea ice
677 conditions and marine transportation activity in Canadian Arctic waters between 1990
678 and 2012, *Climatic Change* 123 (2), 161173.
- 679 Pan, W., A. M. Tartakovsky, and J. J. Monaghan (2013). Smoothed particle hydrody-
680 namics non-Newtonian model for ice-sheet and ice-shelf dynamics. *J. of Comp. Phys.*,
681 242, 828-842.
- 682 Pralong, A., and M. Funk (2005), Dynamic damage model of crevasse opening and appli-
683 cation to glacier calving, *J. Geophys. Res.*, 110, B01309.
- 684 Sergienko, O. V. (2013). Basal channels on ice shelves. *J. of Geophys. Res.: Earth Surface*,
685 118(3), 1342-1355.
- 686 Silva, T. A. M., Bigg, G. R., and Nicholls, K. W. (2006), Contribution of giant icebergs
687 to the Southern Ocean freshwater flux. *J. of Geophys. Res.: Oceans*, 111(C3).

Smith, K., B. Robison, J. Helly, R. Kaufmann, H. Ruhl, H., T. Shaw, and M. Vernet
(2007), Free-drifting icebergs: Hotspots of chemical and biological enrichment in the
Weddell Sea, *Science*, 317, 478482.

Shepherd, A., and D. Wingham (2007). Recent sea-level contributions of the Antarctic
and Greenland ice sheets. *Science*, 315(5818), 1529-1532.

Stern, A. A., D. M. Holland, P. R. Holland, A. Jenkins and J. Sommeria (2014), The effect
of geometry on ice shelf ocean cavity ventilation: a laboratory experiment. *Experiments
in Fluids*, 55(5), 1-19.

Stern, A.A., Johnson, E., Holland, D.M., Wagner, T.J., Wadhams, P., Bates, R., Abra-
hamsen, E.P., Nicholls, K.W., Crawford, A., Gagnon, J. and Tremblay, J.E. (2015),
Wind-driven upwelling around grounded tabular icebergs. *J. of Geophys. Res.: Oceans*,
120(8), 5820-5835.

Stern, A. A., A. Adcroft, and O. Sergienko (2016), The effects of Antarctic iceberg calv-
ing?size distribution in a global climate model. *J. of Geophys. Res.: Oceans*, 121(8),
5773-5788.

Swope, W. C., H. C. Andersen, P. H. Berens, and K. R. Wilson (1982), A computer
simulation method for the calculation of equilibrium constants for the formation of
physical clusters of molecules: Application to small water clusters. *The Journal of
Chemical Physics* 76, no. 1, 637-649.

Tournadre, J., N. Bouhier, F. Girard-Ardhuin, and F. Rmy (2016), Antarctic icebergs
distributions 1992-2014. *J. Geophys Res: Oceans*.

Turnbull I.D., N. Fournier, M. Stolwijk, T. Fosnaes, D. McGonigal (2015), Operational
iceberg drift forecasting in Northwest Greenland, *Cold Reg. Sci. Technol.* 110, 1-18

- 711 Unger, J. D., 2014. Regulating the Arctic Gold Rush: Recommended Regulatory Reforms
712 to Protect Alaska's Arctic Environment from Offshore Oil Drilling Pollution . *Alaska L.*
713 *Rev*, 31
- 714 Vernet, M., et al. (2012), Islands of ice: Influence of free-drifting Antarctic icebergs on
715 pelagic marine ecosystems, *Oceanography*, 25(3), 3839
- 716 Weeks, W. F., and W. J. Campbell (1973). Icebergs as a fresh-water source: an appraisal.
717 *J. of Glaciol.*, 12(65), 207-233.
- 718 White, L., A. Adcroft, and R. Hallberg (2009), High-order regridding remapping schemes
719 for continuous isopycnal and generalized coordinates in ocean models. *J. of Comp.*
720 *Phys.*, 228(23), 8665-8692.

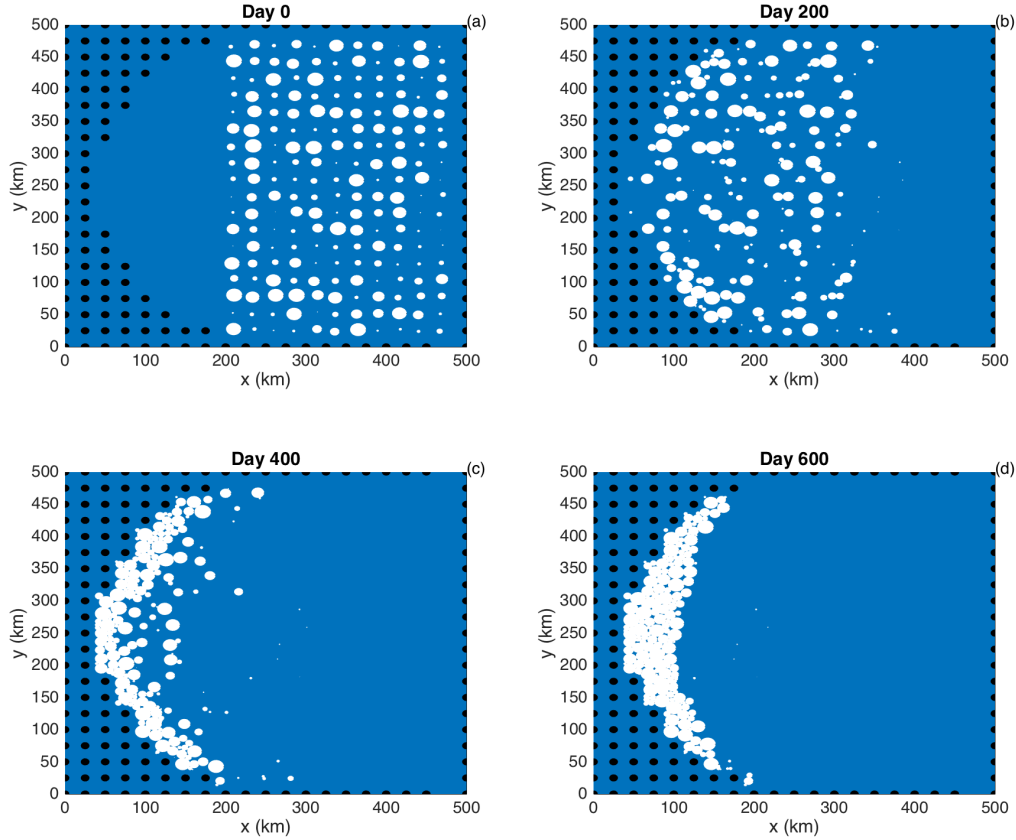


Figure 1. Results of an ice-only LIISM simulation with no bonds between ice elements. Ice elements are initialized throughout the domain, as shown in panel (a). The elements are forced by an imposed westward ocean current of $u=0.1\text{m/s}$ (no ocean model is used). Forces due to sea surface slope, atmospheric drag, Coriolis and sea ice drag are set to zero. The figure shows snapshots of ice element positions at time (a) $t=0$, (b) 200, (c) 400, (d) 600 days. The size of the dots shows the surface area (and interaction diameter) of each ice element. Land points are shown by black circles.

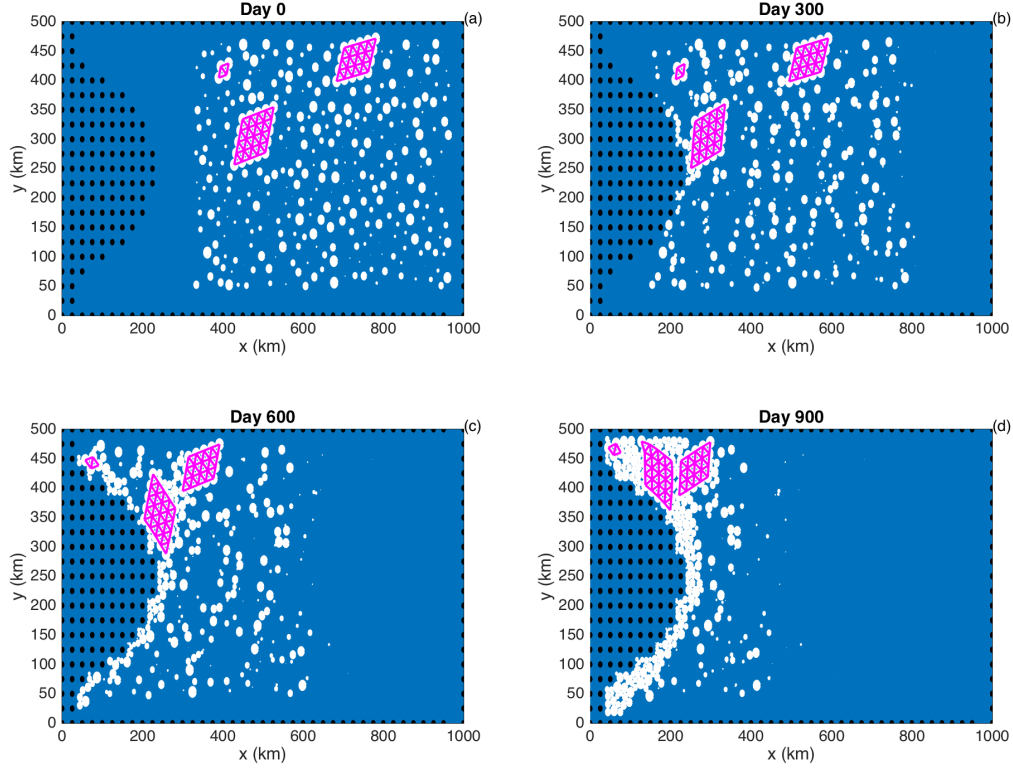


Figure 2. Results of an ice-only LIISM simulation using bonds between elements. Ice elements are initialized throughout the domain, as shown in panel (a). Three tabular icebergs are included, with 25, 16 and 4 elements respectively. The elements are forced by an imposed westward ocean current of $u=0.1\text{m/s}$ (no ocean model is used). Forces due to sea surface slope, atmospheric drag, Coriolis and sea ice drag are set to zero. The figure shows snapshots of ice element positions at time (a) $t=0$, (b) 300, (c) 600, (d) 900 days. The size of the dots shows the surface area (and interaction diameter) of each ice element. Bonds between ice elements are plotted in magenta. Land points are shown by black circles.

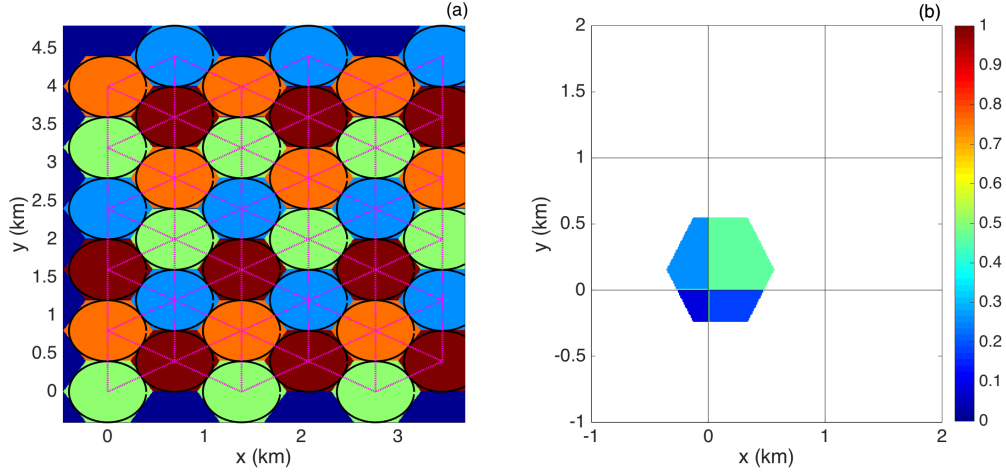


Figure 3. (a) Hexagonal elements are initialized in a staggered lattice as shown. Adjacent elements are bonded together. The centers of bonded elements are plotted in pink. The element bonds form equilateral triangles which give the larger structure rigidity. The black circles show the interactive length scales used in element interactions. (b) Intersection of a hexagonal element and an ocean grid. The colors indicate the fraction of the hexagon that lies in each grid cell. These fractions are used as weights to spread LIISM properties to the ocean grid (see text for more details).

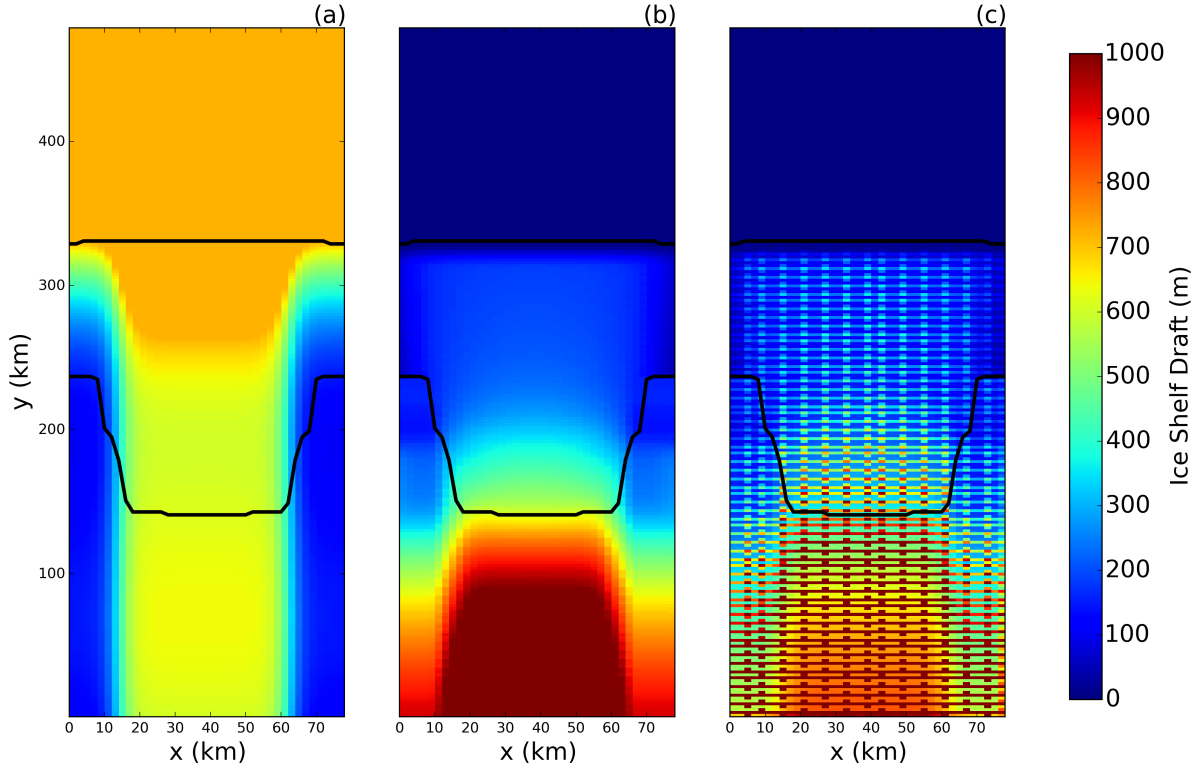


Figure 4. (a) Ocean bottom topography in MISOMIP configuration. (b) ice-shelf draft used in static shelf experiment. The ice draft is calculated from the ice mass in an ocean grid cell, which is found by spreading ice mass across ocean cells accounting for the size of each element (as explained in Section 2.3). (c) Same as in panel (b), except that the interpolation does not account for iceberg size, and instead treats elements as point masses.

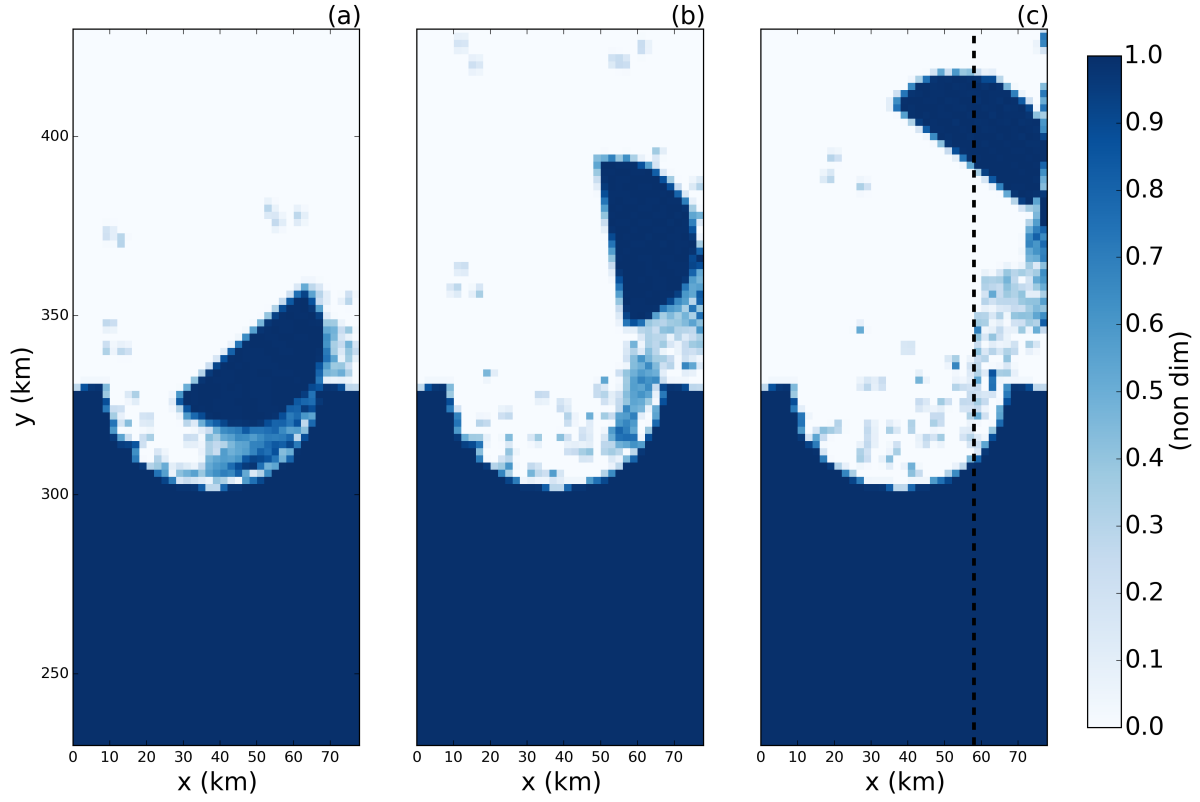


Figure 5. Snapshots of the fraction of ice cover in the LIISM tabular iceberg calving experiment. Snapshots are taken (a) 7, (b) 15, and (c) 30 days after calving. The dashed line in panel (c) shows the location of the vertical transects shown in Figures 6 and 8.

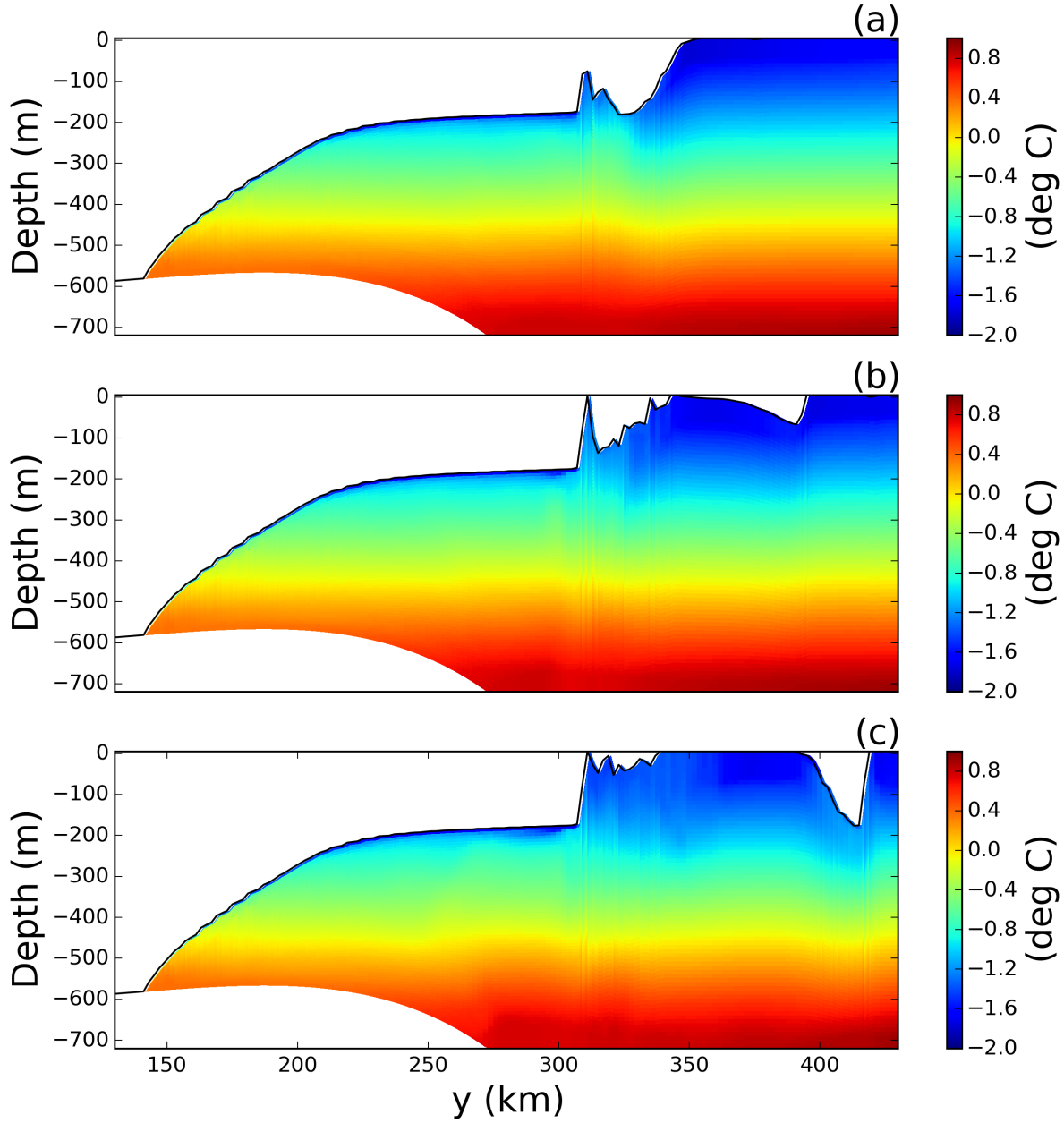


Figure 6. Snapshots of vertical sections of ocean temperature at $x = 58\text{km}$ in the LIISM tabular iceberg calving experiment. Snapshots are taken (a) 7, (b) 15, and (c) 30 days after calving. The position of the vertical transects is shown by the dashed lines in Figure 5c.

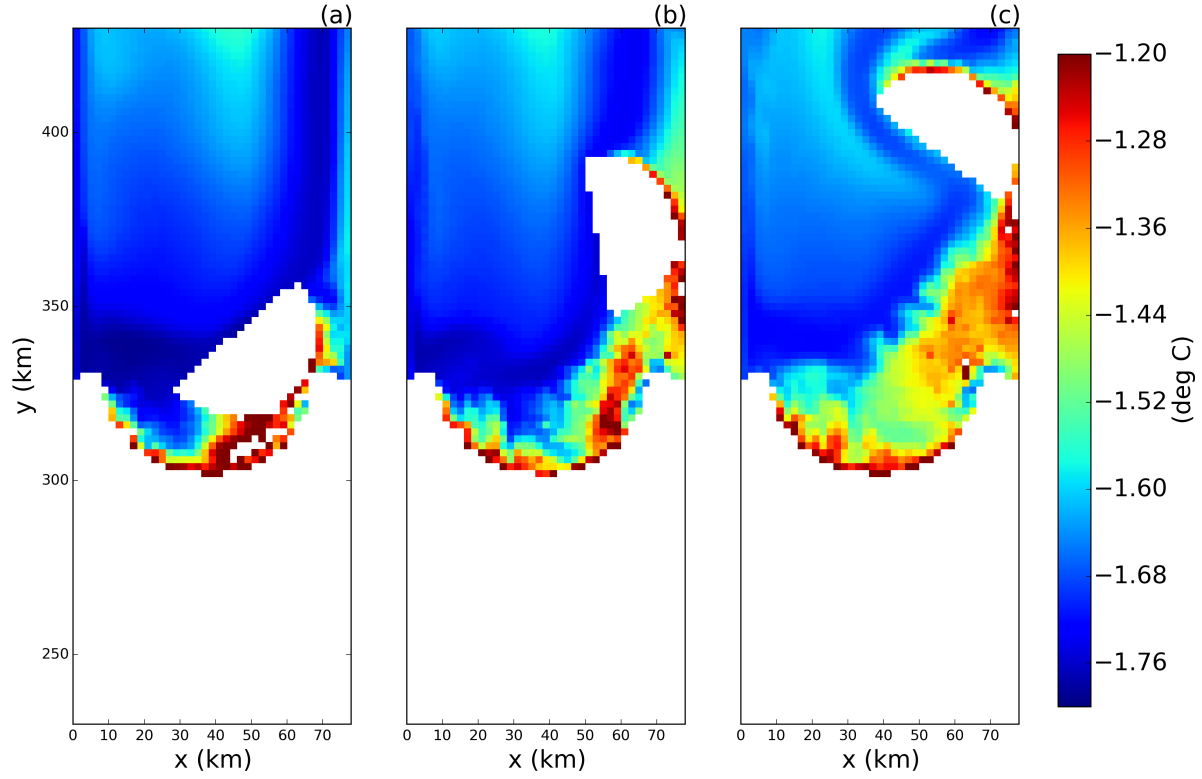


Figure 7. Snapshots of the sea surface temperature in the LIISM tabular iceberg calving experiment. Snapshots are taken (a) 7, (b) 15, and (c) 30 days after calving. Regions with ice area fraction = 1 area plotted in white.

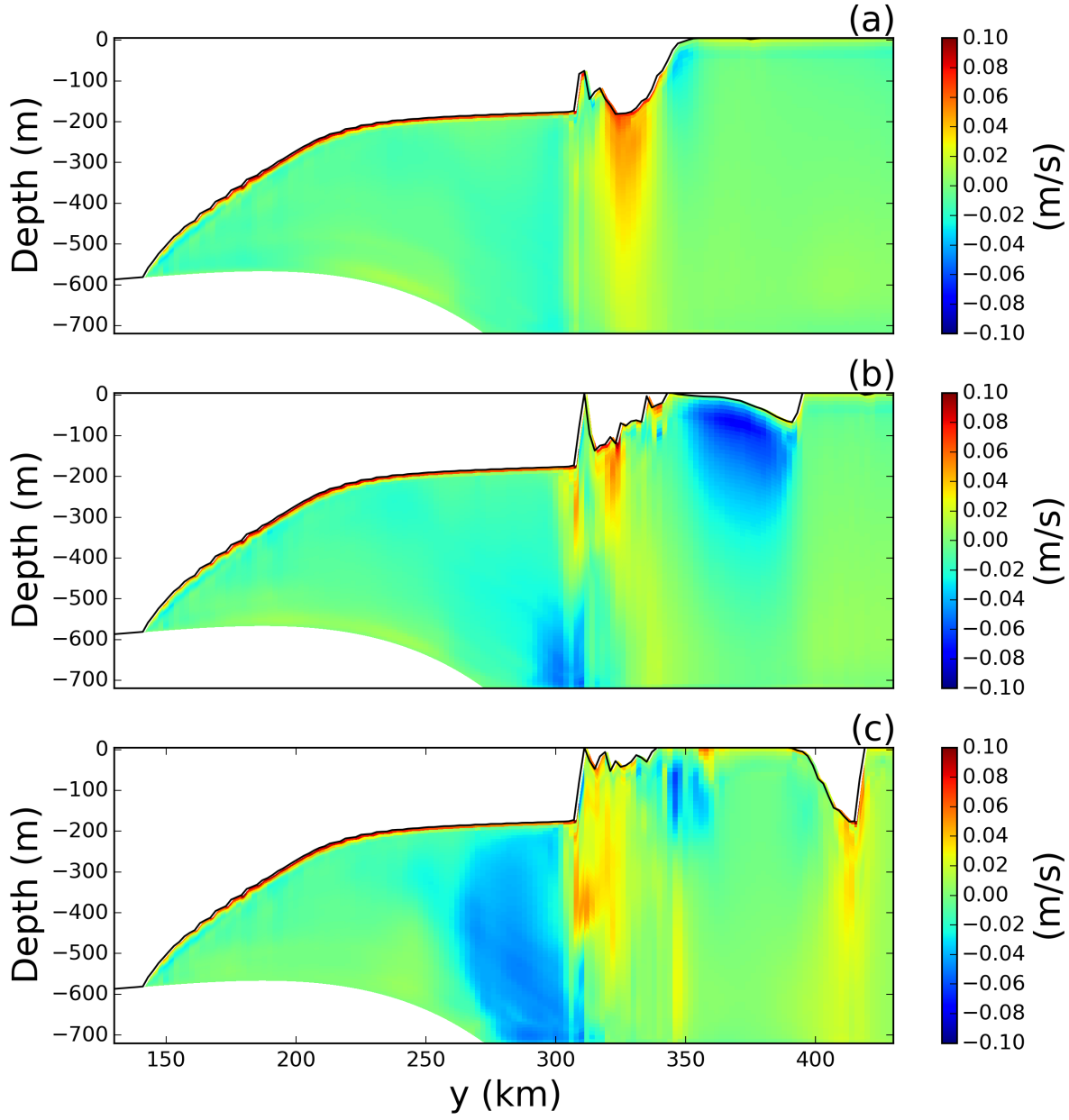


Figure 8. Snapshots of vertical sections of meridional velocity at $x = 58\text{km}$ in the LIISM tabular iceberg calving experiment. Snapshots are taken (a) 7, (b) 15, and (c) 30 days after calving. The position of the transects is shown by the dashed line in Figure 5c.

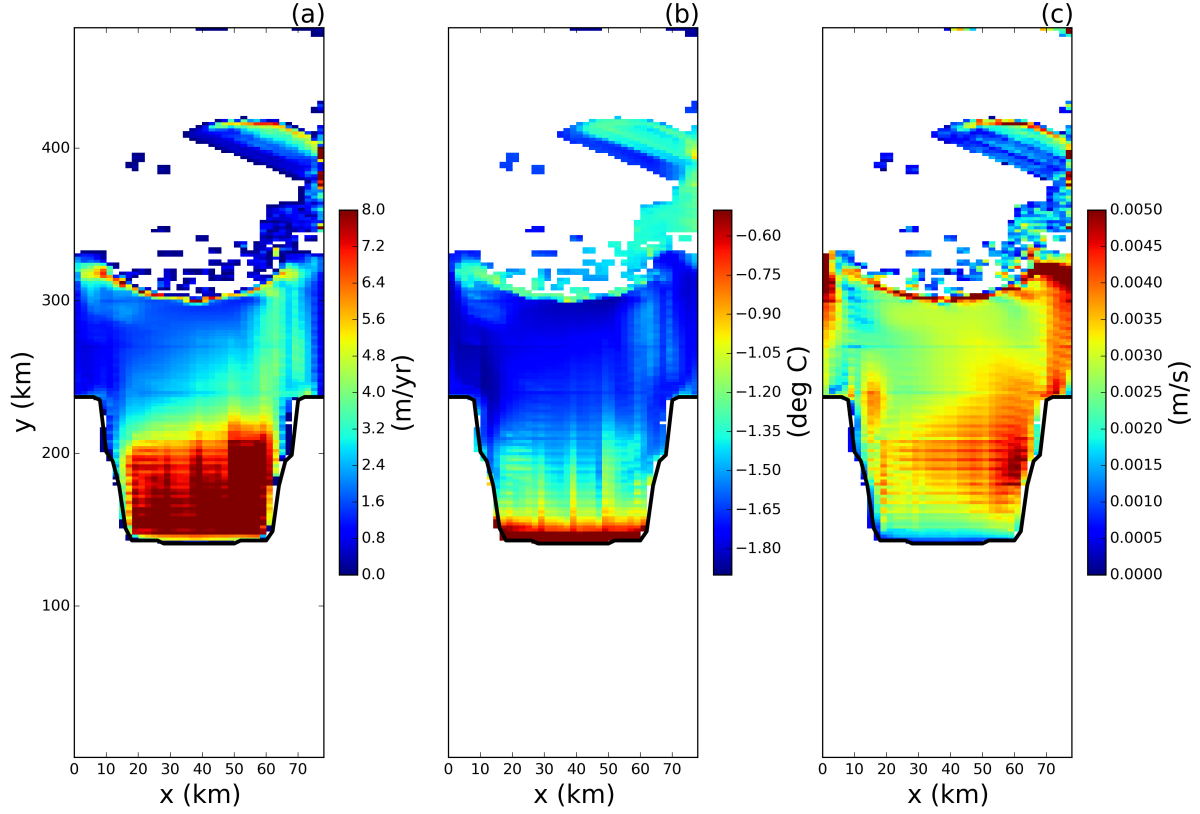


Figure 9. Results of the tabular iceberg calving simulation 30 days after the iceberg calves. The three panels show snapshots of the (a) melt rate, (b) top-of-ocean temperature and (c) u^* at the base of the ice shelf. Fields are only shown in regions where the ice area fraction is ≥ 0.8 .

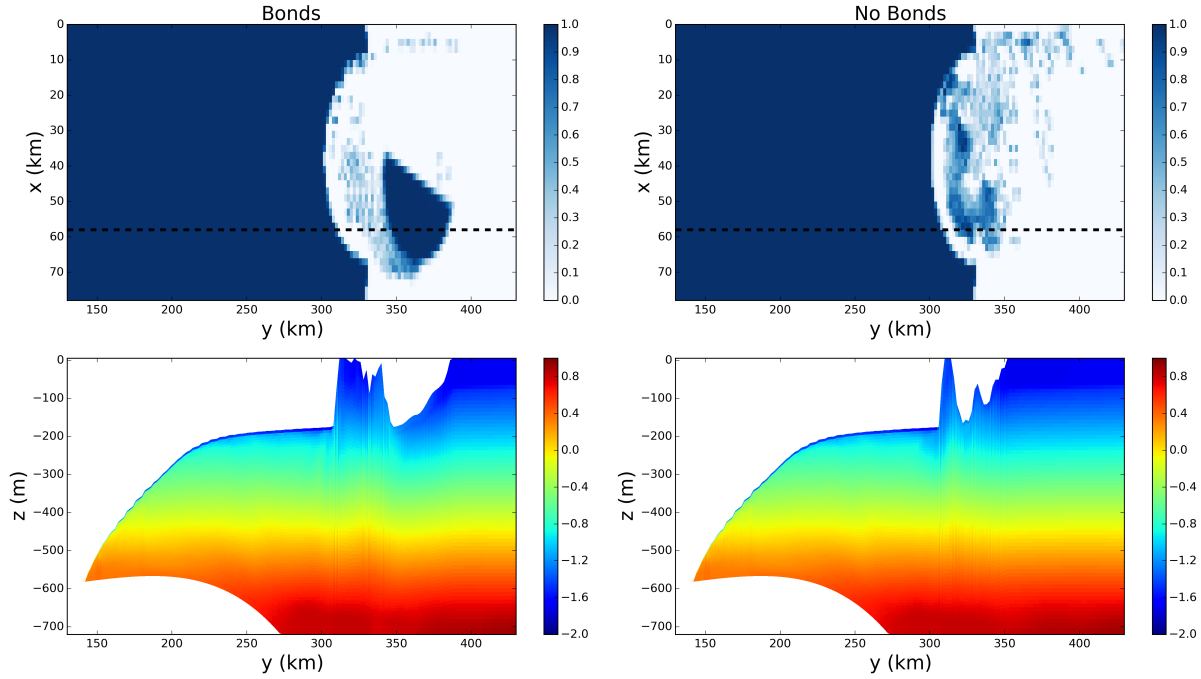


Figure 10. Results from the tabular iceberg calving experiment with and without iceberg bonds. The top row shows the fractional ice cover for the simulations (a) with and (b) without numerical bonds. The bottom row shows the corresponding vertical temperature section at $x = 58\text{km}$ for the simulation (c) with and (d) without bonds. The location of the vertical transects in panels (c) and (d) are shown by the dashed lines in panels (a) and (b), respectively. All snapshots are taken at time $t = 30$ days. The simulations use wind stress $\vec{\tau} = \langle 0.0, 0.05 \rangle$.